1   **Estimation of rainfall erosivity based on WRF-derived raindrop size distributions**

2   Qiang Dai[1,2], Jingxuan Zhu[1], Shuliang Zhang[1], Shaonan Zhu[3], Dawei Han[2] and Guonian Lv[1]

3   [1]Key Laboratory of VGE of Ministry of Education, Nanjing Normal University, Nanjing, China.

4   [2]Department of Civil Engineering, University of Bristol, Bristol, UK.

5   [3]College of Geographical and Biological Information, Nanjing University of Posts and
6   Telecommunications, Nanjing, China

7   Corresponding author: Qiang Dai (qd_gis@163.com)

8   **Key Points:**

9   • Rainfall kinetic energy derived from the Weather Research and Forecasting model offers
10   a novel way to estimate large-scale soil erosion.

11   • Annual rainfall and erosivity are not always positively correlated.

12   • Highest rainfall erosivity of UK occurs in the west coast area during 2013–2017.

13

Abstract

Soil erosion can cause various ecological problems, such as land degradation, soil fertility loss, and river siltation. Rainfall is the primary water-driving force for soil erosion, and its potential effect on soil erosion is reflected by rainfall erosivity that relates to the raindrop kinetic energy. As it is difficult to observe large-scale dynamic characteristics of raindrops, all the current rainfall erosivity models use the function based on rainfall amount to represent the raindrops kinetic energy. With the development of global atmospheric re-analysis data, numerical weather prediction techniques become a promising way to estimate rainfall kinetic energy directly at regional and global scales with high spatial and temporal resolutions. This study proposed a novel method for large-scale and long-term rainfall erosivity investigations based on the Weather Research and Forecasting (WRF) model, avoiding errors caused by inappropriate rainfall–energy relationships and large-scale interpolation. We adopted three microphysical parameterizations schemes (Morrison, WDM6, and Thompson aerosol-aware) to obtain raindrop size distributions, rainfall kinetic energy and rainfall erosivity, with validation by two disdrometers and 304 rain gauges around the United Kingdom. Among the three WRF schemes, Thompson aerosol-aware had the best performance compared with the disdrometers at a monthly scale. The results revealed that high rainfall erosivity occurred in the west coast area at the whole country scale during 2013–2017. The proposed methodology makes a significant contribution to improving large-scale soil erosion estimation and for better understanding microphysical rainfall–soil interactions to support the rational formulation of soil and water conservation planning.

1 Introduction

Soil erosion plays a pivotal role in shaping the Earth's physical landscape; however, it can threaten both ecosystems and human societies (Alewell et al., 2015). Accurate quantification of soil loss impact at large spatial scales is therefore important for developing land-use planning and sustainable conservation practices (Bilotta et al., 2012). The soil erosion rate is driven by a combination of factors, including rainfall, topography, soil characteristics, land cover, and land management applications (Wischmeier and Smith, 1958; Panagos et al., 2015b). Among these, rainfall is a driving force that accounts for a large proportion of soil loss throughout most of the world (Panagos et al., 2015b). The erosive force of rainfall with consequent runoff is represented

as erosivity of rainfall. This is a crucial factor for estimating soil loss in large-scale soil erosion models; for instance, the Universal Soil Loss Equation (USLE (Wischmeier and Smith, 1978) or RUSLE (Renard et al., 1997)), Limburg Soil Erosion Model (LISEM) (De Roo et al., 1996), and USLE-M (Kinnell and Risse, 1998).

Rainfall erosivity estimation involves the microphysical properties of rainfall and rainfall–soil interactions on different time steps (Petan et al., 2010). Impact of rainfall, the main mechanism driving the splashing of soil particles from the soil mass, which leads to soil erosion through soil disintegration and mobilization, relies on the kinetic energy (KE) of raindrop motions (Wischmeier and Smith, 1958; Wang et al., 2014). Robust measurement of raindrop size and terminal velocity is vital for estimating and predicting rainfall erosivity. Many measurements can be used to obtain these two parameters, including the stained paper or flour pellet methods (Marshall and Palmer 1948; Wischmeier and Smith, 1958), high speed cameras (Jones, 1959; Kinnell, 1981; McIsaac, 1990), and disdrometers (Petan et al., 2010; Angulo-Martinez et al., 2012). Accurate measurements of raindrop size can be provided in all their methods, and terminal velocity of raindrops can be further measured by video cameras and disdrometers. Velocity can also be estimated as the function of raindrop diameter from the empirical relationship (Beard, 1976; Atlas and Ulbrich, 1977; Uplinger, 1981; Van Dijk et al., 2002). When using ground observations, rainfall KE can be estimated at a given site.

However, direct measurement of rainfall KE in a large area is difficult because it requires considerable effort, as well as a dense network of expensive instruments that provide accurate outputs (Fornis et al., 2005; Mikoš et al., 2006; Meshesha et al., 2016; Dai et al., 2017). Previous studies have, therefore, mainly employed more readily accessible records like rainfall intensity, and attempted to estimate rainfall KE from the empirical relationship of unit KE (*ke*) with intensity (*ke–I*). Since Marshall and Palmer (1948) first observed a two-parameter exponential relationship between drop size and intensity, several forms of *ke–I* mathematical expressions for specific locations and climatic conditions have been proposed, including power-law (Park et al., 1982; Meshesha et al., 2016), linear (Sempere-Torres et al., 1998; Nyssen et al., 2005), polynomial (Carter et al., 1974), logarithmic (Wischmeier and Smith, 1978; Davison et al., 2005; Meshesha et al., 2014), and exponential (Kinnell, 1981; Brown and Foster, 1987) relationships. Among these, the exponential function has been preferentially used currently (Van Dijk et al., 2002; Fornis et al., 2005; Petan et al., 2010; Sanchez-Moreno et al., 2012; Lim et al., 2015).

75 Accurate raindrop size distribution (DSD) measured by disdrometers is widely used to derive *ke–*
76 *I* relationships (Angulo-Mart ńez et al., 2016; Meshesha et al., 2016). However, such empirically
77 derived formulas indicate that rainfall *ke* will increase infinitely with increasing intensity,
78 whereas studies (Rosewell, 1986; Angulo-Mart ńez et al., 2016; Meshesha et al., 2019) have
79 found that rainfall *ke* reaches an top value when intensity is around 70 mm h^{-1} (Hudson, 1963;
80 Wischmeier and Smith, 1978). More importantly, such a *ke–I* relationship only represents local
81 climate and precipitation microphysics and is valid for such regions. There is great uncertainty
82 associated with rainfall erosivity estimation using this *ke–I* relationship in a large domain
83 (Angulo-Mart ńez and Barros, 2015), especially due to the poor spatial and temporal
84 predictability of the *ke–I* relationship. This has motivated researchers to directly calculate KE
85 based on large-scale DSD measurements.

86 Ground- and space-based radar can be used to obtain DSD parameters (Atlas et al., 1973;
87 Doelling et al., 1998). For example, the space-borne Dual-frequency Precipitation Radar (DPR)
88 radar containing Ku- and Ka-bands in the Global Precipitation Measurement (GPM) satellite
89 allows researchers to estimate the global three-dimensional spatial distribution of hydrometeors.
90 Unfortunately, ground dual-polarization radars are available in limited areas (Prigent, 2010) with
91 large uncertainties (Dai et al., 2019), and the GPM DPR instrument, which measures DSD with
92 daily or longer temporal resolutions, fail to capture a full storm and meet the requirement for
93 rainfall kinetic estimation. Mesoscale numerical weather prediction models, for instance, the
94 WRF model, can simulate microphysical cloud processes and predict the evolution of particle
95 size distribution through computationally feasible parametrization schemes (Dai et al., 2014;
96 Brown et al., 2016). DSD on the ground can be derived from the WRF model through
97 consideration of various physical processes, types of hydrometeor, and free degrees of size
98 distributions in hydrometeor. As such, a number of recent researches have investigated the
99 retrieval and uncertainty of DSD parameters by WRF (Gilmore et al., 2004; Ćurić et al., 2009;
100 Brown et al., 2016; Yang et al., 2019).

101 The WRF model runs with initial and boundary conditions using global reanalysis
102 datasets, such as those of the European Centre for Medium-range Weather Forecasts (ECMWF)
103 and National Centers for Environmental Prediction (NCEP). In other words, WRF-derived DSD
104 can be obtained for any given area with fine spatial and temporal resolutions rather than
105 traditional course linear interpolations. We therefore attempted to estimate rainfall erosivity for

106   the entirety of the United Kingdom (UK) domain using WRF-derived DSD. For comparison, we

107   also calculated interpolated traditional disdrometer-derived rainfall erosivity. To our knowledge,

108   this work is the first attempt to take advantage of a numerical weather prediction model for

109   estimating rainfall erosivity anywhere around the world. The current study contributes to the

110   development of large-scale soil erosion estimation and provides a better comprehension of

111   microphysical rainfall–soil interactions.

2 Methodology

112

2.1 Disdrometer-based rainfall KE estimation

113

114   KE dominates the ability of raindrops to separate soil particles. The KE (e, unit: J) of a

115   raindrop with mass m (g) and terminal velocity v (m s^{-1}) is defined by:

$$e = \frac{1}{2} mv^2 \tag{1}$$

116   Assuming a spherical volume for every raindrop shape, the mass of a drop can be

117   calculated from the cube of the diameter D (mm). Because instruments (e.g., disdrometers)

118   generally sample drop size, the mean radius and falling velocity of the corresponding sampling

119   drop-size class are used to represent D and v, expressed as D_i and v_i, respectively. In such cases,

120   the e_i with any drop of a given class is given as:

$$e_i = \frac{1}{12} 10^{-6} \pi \rho v_i^2 D_i^3 \tag{2}$$

121   where ρ is the water density (g cm^{-3}). The sum of the KE of each individual raindrop within a

122   given rain depth that hits a given area defines the total KE. The unit rainfall KE ke_t in the tth

123   minute (MJ ha^{-1} mm^{-1}) can be calculated as the sum of each drop KE in each size set, as follows:

$$ke_t = \frac{e_{sum}}{AP_t} = \frac{1}{AP_t} \sum_{i=1}^{ni} N_i e_i \tag{3}$$

124   where A represents the sample area of the sensor, P_t is rainfall depth at time t, and N_i is the drops

125   number in class i. The instrument sums up the number of raindrops in each sampling class and

126   produces the raindrop spectra for a time step. Here, we use the term ke to represent the

127   disdrometer-based KE estimated by DSD directly measured every minute. The terminal velocity

128 of a raindrop can be estimated from its power law empirical relationship with raindrop diameter

129 (Atlas and Ulbrich, 1977), with this considered more suitable for Chilbolton in the UK (Islam et

130 al., 2012):

$$V_{At1} = 3.78D_i^{0.67} \tag{4}$$

131 Thus, unit rainfall KE estimates per minute are obtained by replacing v_i in Eq. (2) with v_{Atl}.

132 The other form of rainfall KE is expressed at an event scale and represents the sum of the

133 storm energy covering all time steps covering an event. The individual event energy (MJ ha^{-1}) is

134 calculated as follows:

$$E = \sum_{t=1}^{nt} ke_t P_t \tag{5}$$

135 where P_t is the rainfall amount (mm) in the tth minute and nt is the time steps number. Historical

136 rainfall data are divided into wet and dry periods. A string of erosive rainfall storms is first

137 extracted through the predefined rules. A continuous 6-h dry period interval was used to divide

138 rainfall events (Hanel et al., 2016), following the "minimum dry-period duration" definition of a

139 rainfall event (Bonta, 2004). Moreover, a rainfall amount of 12.7 mm was set as the threshold to

140 filter effective rainfall events (Renard et al., 1997).

141 Rainfall KE is obtained for a given site based on size and velocity of raindrops. When

142 disdrometer data are absent, energy can be estimated from empirical relationships using rainfall

143 intensity I (mm). Five commonly used functions (including exponential, logarithmic, power law,

144 and inverse proportion) have been mentioned in Section 1. Taking the exponential form as an

145 example, the rainfall KE at any location can be estimated as:

$$E_{max} = e_{max}(1 - ae^{-bI}) \tag{6}$$

146 where e_{max} is the mean maximal value of energy measured under high rainfall intensity, and a

147 and b are coefficients modeling the equation curve. Here, minimum KE can be determined by

148 parameters a and e_{max} together, while the overall shape of the curve is modeled by parameter b.

149   2.2 WRF-based rainfall KE estimation

150   Differing from disdrometer measurements, the complete DSD cannot be obtained from

151   the WRF model. Instead, the DSD of the microphysical parameterization (MP) scheme is

152   handled with a constrained-gamma distribution model, which is defined as:

$$N(D) \ = \ N_0 D^{\mu} e^{-\lambda D} \tag{7}$$

153   where N_0, μ, and λ are the intercept, shape, and slope parameters of the DSD. In terms of

154   double-moment bulk schemes, N_0 and λ can be abstracted from the number concentration N and

155   predicted mixing ratio q, as shown below:

$$N_0 \ = \ \frac{N\lambda^{\mu+1}}{\Gamma(\mu \ + \ 1)} \tag{8}$$

$$\lambda \ = \ \left[\frac{cN\Gamma(\mu \ + \ d \ + \ 1)}{q\Gamma(\mu \ + \ 1)} \right]^{\frac{1}{d}} \tag{9}$$

156   c and d are the assumed power-law coefficients between diameter and mass ($m \ = \ cD^d$), and Γ

157   represents the function in gamma form (Morrison et al., 2009). The value of the shape parameter

158   μ ($\mu \ = \ 0$) in double-moment schemes is fixed, except for the WRF double-moment 6-class

159   (WDM6) schemes, following gamma distribution, which defined $\mu \ = \ 1$ (Jung et al., 2010;

160   Johnson et al., 2016).

161   Because DSD retrieval is sensitive to MPs (Cintineo et al., 2014; Morrison et al., 2015),

162   the WRF model this study adopted completely or partially three types of double-moment cloud

163   MP schemes. The Morrison double-moment scheme involves the number concentrations and

164   mixing ratios of multiple hydrometeors (Morrison et al., 2009). Moreover, the WDM6 scheme

165   further considers a prognostic factor to estimate and predict the cloud condensation nuclei (CCN)

166   number concentration (Hong et al., 2010; Lim and Hong, 2010). Finally, the Thompson aerosol-

167   aware (TAA) scheme can predict both ice nuclei (IN) and CCN number concentrations

168   (Thompson and Eidhammer, 2014).

169   The DSD parameters were thus obtained under the three WRF MPs. For theoretical DSD,

170   *ke* estimates per minute were obtained by integration of the full raindrop size spectrum using:

$$ke'_t = \frac{1}{AR_t} \int_0^\infty N(D) \frac{1}{12} 10^{-6} \pi \rho v_i^2 D_i^3 dD \tag{10}$$

171   For the WRF-derived DSD covering the whole study area, there was no need to construct

172   a ke–I relationship to interpolate KE in ungauged areas. The WRF-based rainfall KE under storm

173   event scale is thus given as:

$$E_W = \sum_{t=1}^{nt} ke'_t \, P_t \tag{11}$$

174   2.3 Rainfall erosivity estimation

175   Most storm events have relatively low intensities and KEs with occasional peaks, based

176   on the disdrometer DSD data used to evaluate the rainfall ke–I function. Proper estimation of

177   rainfall erosivity potential should consider total KE over a long period. The rainfall erosivity

178   factor (or R-factor) is calculated by a multi-annual average of the total storm erosivity index

179   (Wischmeier and Smith, 1958; Van Dijk et al., 2002), while annual rainfall erosivity R can be

180   obtained using:

$$R = \sum_{m=1}^{M} (EI_{30})_m \tag{12}$$

181   where M is the total number of erosive events within a year. $(EI_{30})_m$ are total rainfall kinetic

182   energy and maximum 30-min rainfall intensity recorded within 30 consecutive minutes (unit:

183   mm h^{-1}), respectively, for the mth event.

184   Wischmeier and Smith (1958) first proposed the use of EI_{30}, as the rainfall erosivity for

185   each event, based on research data from many sources. I_{30} was calculated to have higher

186   relevance to soil erosion than maximum 5-min, 15-min, or 60-min rainfall intensities

187   (Wischmeier and Smith, 1958). The calculation of EI_{30} initially uses recording-rain gauge data to

188   divide continuous rainfall into time periods with equal rainfall intensity. Though rainfall

189   measurements with high temporal resolutions are required, it is difficult to obtain them from

190   general rainfall measurements. Therefore, short time equal-interval rainfall data with higher

191   accuracy over multiple years are preferred for estimating EI_{30}. For example, Xie et al. (2016)

192   used 1-min rainfall data instead of recording-rain gauge records. For coarse-resolution, equally

193 spaced data, researchers have proposed a conversion factor to reduce bias error (Weiss, 1964;
194 Williams and Sheridan, 1991).

195 The rainfall erosivity can be derived from rainfall KE. It plays a main dynamic role in
196 USLE/RUSLE, representing the potential for soil erosion caused by rainfall. To distinguish the
197 disdrometer- and WRF-derived rainfall erosivity in this study, we use the terms R_D and R_W,
198 respectively.

199 2.4 Evaluation methods

200 Because there is no direct way to measure rainfall erosivity across a large area, it is
201 difficult to validate outcomes using observations. However, R_D is considered to be relatively
202 accurate due to its specific measurement of raindrops. We therefore assumed that R_W values were
203 accurate if it closely matched R_D of a given location. A long-term comparison of R_W and R_D at
204 disdrometer stations was thus conducted to evaluate the validity of R_W.

205 Three indicators were introduced for the evaluation: Pearson's correlation coefficient,
206 mean absolute error (MAE), and coefficient of determination (R^2) (Borrelli et al., 2017). Pearson
207 correlation coefficient is an index used to evaluate the linear correlation between two variables,
208 and is defined as follows:

$$Pearson = \frac{n\sum R_{D_i}\sum R_{W_i} - \sum R_{D_i}\sum R_{W_i}}{\sqrt{n\sum R_{D_i}^2 - (\sum R_{D_i})^2}\sqrt{n\sum R_{W_i}^2 - (\sum R_{W_i})^2}} \tag{13}$$

209 where n is the number of variable samples. Because this correlation cannot reveal the absolute
210 bias of rainfall erosivity values, the MAE was also used; this is defined as:

$$MAE = \frac{\sum |R_{W_i} - R_{D_i}|}{n} \tag{14}$$

211 R^2 is an indicator to assess the fit of the trend line, expressed as the ratio of the variance
212 in the dependent variable predicted from the independent variable. It measures the extent to
213 which the model replicates observations based on the proportion of the results interpreted by the
214 model to the total change, written as:

$$R^2 = 1 - \frac{SS_{res}}{SS_{tot}} \qquad (15)$$

215 where SS_{res} is the sum of squares of residuals between two variables, and SS_{tot} is the total sum of
216 squares.

3 Study area and data sources

218 The whole of the UK was set as the experimental area for investigating rainfall erosivity
219 estimation. The UK consists of mostly lowland terrain, with a maximum elevation of 1345 m.
220 Water and wind are the most significant forces of soil erosion in the UK. Together, they cause
221 approximately 2.2 million tons of topsoil to be eroded annually, seriously affecting soil
222 productivity, water quality, and aquatic ecosystems through siltation of watercourses (EA, 2004).
223 According to the Environmental Agency, the total cost of soil erosion in the UK is approximately
224 $88 million each year, including an agricultural production loss of $17.6 million (O'Neill, 2007).
225 More importantly, the changing climate may exacerbate the degree of erosion. For example,
226 hotter, drier climates make soils more susceptible to wind erosion, and intense storms increase
227 rainfall erosivity (Defra, 2009). Studies of water erosion in England and Wales (Morgan, 1985;
228 Evans, 1990) have found that loose soils (especially sand), such as the soils found in Shropshire
229 and Herefordshire in Wales, are more susceptible to water erosion. In a study of rainfall erosion
230 in Europe, Panagos et al. (2015a) found that the humid Atlantic climate results in highly variable
231 rainfall erosivity, such as higher R-factor values in western England and lower values in the
232 eastern UK.

233 The gauge datasets used are from the land surface and marine surface measurements
234 datasets (data availability: 1853–present) provide by the UK Met Office. A network of rain
235 gauges covering 304 stations across the whole UK observes continuous rainfall data in hours
236 (Figure 1). The base data of most stations comprises the times of each tip (0.2 mm per tip),
237 converted into 1-h rain accumulations. The rainfall observations are not always valid for each
238 hour at each station. The hourly grid-based rainfall maps are then calculated based on ordinary
239 kriging interpolation of rain gauge network data to obtain the spatial distribution of rainfall for
240 each time step, as inputs for rainfall erosivity estimation. This wide-range-use geostatistical
241 approach can account for both the distance and pairwise spatial relationship between points

through variograms. The precipitation interpolation method uses sample gauge points taken at different locations and creates a continuous surface to achieve an accurate spatial variation estimation of rainfall patterns.

We used data from two disdrometers in southern England. The first was Chilbolton station (51°08'N, 1°26'W), with an impact-type Joss–Waldvogel disdrometer (JWD) mainly used to compute rainfall erosivity. It can measure drop sizes from 0.3 to 5.0 mm in 127 bins. The sampling period and collector area were 10 s and 50 cm^2, respectively. Data were available for April 2003 to July 2018. The second was the University of Bristol station (51°27'N, 2°36'W), with an OTT Parsivel^2 disdrometer (OPD). Data were available for November 2015 to December 2018. This disdrometer subdivides particles into appropriate classes and has a nominal cross-sectional area of 54 cm^2. The 10-s period measurement data from the two disdrometers were averaged into a 1-min period to filter out time variations (Montopoli et al., 2008; Islam et al., 2012; Song et al., 2017).

Meteorological data comes from the ERA-Interim dataset, a global atmosphere re-analysis product, generated by the ECMWF. For the scientific community, ERA-Interim is considered to be one of the most important atmospheric datasets, with its data-rich period available since 1979 and updated in current time (Dee et al., 2011). The Integrated Forecasting System released in 2006 contains a 12-h analysis window derived 4-D variational analysis, driving the data assimilation system to generate ERA-Interim. The dataset covers 60 vertical classes of approximately 80 km from the ground to 0.1 hPa. The Gridded Binary format is used to store data for three months in a separate file. A data processing scheme was established to collect and retrieve ERA-Interim data of each rainfall event.

The rain gauge and Chilbolton disdrometer datasets can be obtained from British Atmospheric Data Centre in National Centre for Atmospheric Science research center (MO, 2012). ERA-Interim data can be obtained from the ECMWF Public Dataset website (https://apps.ecmwf.int/). Considering the availability of the above datasets and model requirements, we mainly used data covering the period 2004–2017.

4 Results

4.1 Empirically derived rainfall erosivity estimation

To evaluate the R_W, the raindrop spectrum collected by the Chilbolton station disdrometer is used to estimate rainfall KE first. The key in estimating rainfall KE by disdrometer lies in building an empirical relationship between rainfall amount and KE. We used DSD measurements from 2004 to 2013 to establish five empirical relationships between unit rainfall kinetic energy (*ke*) and intensity (*I*) (Table 1) and used 2014–2017 data for the cross-validation. It can be seen from Table 1 that the inverse proportional relationship (Equation III) had the worst performance, in that both the calibration and validation R^2 values were < 0.3. The values of the other equations were > 0.48, among which the exponential formula (Equation I) had the highest calibration R^2 (0.50) and validation R^2 (0.45), respectively. In addition, the power law formula (Equation V) showed a similar performance to the exponential formula at rainfall intensities < 5 mm h^{-1}. However, the power law formula also had a continuously increasing trend, which may not be suitable for high-intensities. Figure 2 shows the *ke*–*I* relationship and five fitted curves at Chilbolton station. It can be seen that the two logarithmic curves (Equation II and IV) invariably overlap. The logarithmic form has been used for a long time in USLE (Wischemier and Smith, 1978). It describes *ke* well at both low and high *I*, but does not have an upper limit. The power law curve (Equation V) can predict *ke* well at lower *I* but overestimates *ke* at high *I*. The exponent-based relationship (Equation I) is widely used in the literature and in forecast models such as RUSLE (Renard et al., 1997), which fits the data particularly well in Figure 2. Even though *ke* in exponential curve has a minimum value at very low *I*, it also should be noted that higher rainfall intensities are much more important in determining overall storm energy than lower intensities. Therefore, we adopted it here as the empirical formula to estimate rainfall erosivity in the UK.

Based on rainfall KE, the point R_D can be obtained at a disdrometer location. In the current study, we established a method to estimate the *R* using 60-min rainfall data. EI_{30} obtained from 1-min DSD data was considered as the standard *R* at Chilbolton Station. Hourly rain gauge data at the same location were used to calculate $(EI_{30})_{60}$, which refers to EI_{30} calculated from 60-min data. The regression relationship between EI_{30} and $(EI_{30})_{60}$ was then established. The $(EI_{30})_{60}$ of each month, obtained from the 60-min rainfall data of the Chilbolton Station rain gauge in

299 2004–2013, was calculated. The regression relationship between the monthly sum of $(EI_{30})_{60}$ and

300 the standard monthly EI_{30} from DSD was calculated to obtain a coefficient of 1.836. Rainfall

301 erosivity can subsequently be calculated by multiplying $(EI_{30})_{60}$ by the coefficient.

302 Beyond assuming that the disdrometer-derived *ke–I* relationship can be applied to a

303 whole study area; point rainfall measurements must be interpolated to obtain areal rainfall values

304 in traditional rainfall erosivity estimation. We obtained 60-min rainfall data from 304 rain gauges

305 around the UK from 2004 to 2017. Note that not all rain gauges were available for the whole

306 period (available gauges each year are indicated in Figure 3). We used the ordinary kriging

307 interpolation method to obtain the spatial distribution of rainfall for each time step. This wide-

308 range-use geostatistical approach can account for both the distance and pairwise spatial

309 relationship between points through variograms. Figure 3 shows the results of annual rainfall

310 (*Rain*), annual rainfall kinetic energy (*E*), and annual rainfall erosivity (*R*) for different years.

311 The distribution trends of *Rain*, *E*, and *R* were similar, and positively correlated except for

312 certain locations or periods. For instance, in 2013, *Rain* in the northwestern UK decreased from

313 west to east, while E and *R* decreased from south to north; furthermore, areas with large *E* and *R*

314 values in southeastern UK could not be directly observed from the rain map.

315 The key concern in traditional rainfall erosivity estimation is the spatial predictability of

316 the *ke–I* relationship. To verify the regional reliability of this relationship, we used data from a

317 newer disdrometer located at the University of Bristol, approximately 87 km from Chilbolton

318 Station. The validation data at Bristol Station discontinuously covered the period 2016–2019.

319 Figure 4 shows the exponential relationship of *ke–I* at Bristol station, which differed

320 substantially from that based on data from Chilbolton station. A comparison of the modeled and

321 observed event rainfall erosivity is shown in Figure 5. The modeled erosivity of rainfall event

322 was not consistent with the observed event rainfall erosivity. The linear regression coefficient

323 between these values was > 1.2, which was the result of the low *ke* for Bristol Station, and R^2

324 was < 0.85, indicating considerable uncertainty associated with disdrometer-based rainfall

325 erosivity estimation.

326 In summary, the point rainfall erosivity estimated by disdrometer is considered to be

327 accurate compared to other methods. However, a large-scale rainfall erosivity through a simple

328 interpolation of rainfall KE is subjected to a significant uncertainty. In the following analysis, the

329   point R_D is used to appraise the performance of the proposed WRF-based estimated method, and

330   the R_D in the whole UK is only be used for a general comparison of spatial and temporal

331   distribution of rainfall erosivity.

332   4.2 Rainfall and DSD estimation by WRF

333   We used the WRF model ver. 3.8, which has an Advanced Research WRF dynamical

334   core, to downscale the ERA-Interim reanalysis data. The double-nested domain configuration

335   used in the WRF model was centered at 55 °19'N, 2 °21'W and applied at a downscaling ratio of

336   1:5, a finest grid of 5 km, and a temporal resolution of 1 h. Table 2 lists the detailed parameters

337   used in this domain configuration. With the top pressure level set at 50 hPa in each, both

338   domains include 28 vertical levels. To obtain favorable initial weather conditions, the model ran

339   continuously to obtain five years of WRF simulation results.

340   Simulations were performed using three different bulk double moment MPs: the

341   Morrison (Morrison et al., 2009), WDM6 (Hong et al., 2010; Lim and Hong, 2010) and TAA

342   (Thompson and Eidhammer, 2014) schemes. All three can predict the number concentration and

343   hydrometeors mixing ratio for each time step. The WDM6 scheme also predicts the number

344   concentration of CCN (Hong et al., 2010; Lim and Hong, 2010), while the TAA scheme are able

345   to predict both IN and CCN number concentrations (Thompson and Eidhammer, 2014).

346   Additionally, other physical parameterizations include the Dudhia shortwave radiation scheme

347   (Dudhia, 1989), Mellor–Yamada–Janjic planetary boundary layer scheme (Janjić, 1994), RRTM

348   longwave radiation scheme (Mlawer et al., 1997), the Noah land-surface model (Ek et al., 2003),

349   and the Kain–Fritsch cumulus scheme (Kain, 2004),.

350   The median volume diameter parameter (D_0) and generalized intercept parameter (N_w)

351   are generally used in the DSD model of WRF (Islam et al., 2012).

$$N_W = \frac{N_0 D_m{}^\mu}{f(\mu)} \tag{16}$$

$$f(\mu) = \frac{6(4 + \mu)^{\mu+4}}{4^4 \Gamma(\mu + 4)} \tag{17}$$

352   where D_m is the mass-weighted mean diameter. The $f(\mu)$ is a function of the shape parameter μ.

353   The parameter μ is assumed as zero or one (based on microphysical scheme configuration) in

WRF. Figure 6 displays the spatial distribution of D_0 and generalized intercept parameter N_w for a given day with rainfall countrywide (January 10, 2013). D_0 and N_w had similar patterns and were mainly distributed across the southwestern and northeastern UK. The white strip in the middle of Figure 6 represents an area that received no rain. However, the three MPs yielded large differences; D_0 of MP-TAA was the highest among three MPs, whereas N_w of MP-WDM6 was significant larger than the others. In addition, D_0 and N_w did not consistently show a positive correlation. The different MP estimation results underscore the complexity of the rainfall process, which is the reason we estimated rainfall KE using WRF schemes instead of traditional formulas.

4.3 Comparison of WRF- and disdrometer-derived rainfall erosivity at Chilbolton station

With the WRF-based rainfall intensity and DSD estimations, rainfall erosivity was derived using Equations (10)–(12). Hereafter, this is referred to as R_W, which is further distinguished based on the three MP schemes used: $R_{W\text{-}Morrison}$, $R_{W\text{-}WDM6}$, and $R_{W\text{-}TAA}$. Figure 7 compares disdrometer- and WRF-derived monthly rainfall erosivity estimations at Chilbolton station for the period 2014–2017. The general patterns of the four rainfall erosivity values were similar. $R_{W\text{-}Morrison}$ tended to be larger than R_D in some months, whereas $R_{W\text{-}TAA}$ matched the R_D value relatively well for smaller values. Because WRF data were taken from a 2×2-km grid around Chilbolton station, there was a spatial error in addition to the systematic error of estimating rainfall erosivity. Based on the four-year data, the study area is rainy throughout the year with little R monthly, or seasonal patterns change (Figure 8), influenced by the temperate oceanic climate. Figure 8 also indicated that through the perspective of monthly average results, $R_{W\text{-}WDM6}$ values are low, $R_{W\text{-}TAA}$ has a good similarity with low R_D, and $R_{W\text{-}Morrison}$ is the closest to R_D in value.

Table 3 shows the correlation indicator results between monthly R_D and the three types of R_W at Chilbolton station. The Pearson correlation coefficients generally exceeded 0.7, supporting the potential utility of WRF-based estimation. In terms of MAE, $R_{W\text{-}TAA}$ had the best performance (6.51), whereas $R_{W\text{-}Morrison}$ and $R_{W\text{-}WDM6}$ showed slightly worse performance (approximately 8). Among the three schemes, $R_{W\text{-}TAA}$ had the best fit with R_D. The indicators and comparison results suggest that the deviations in results need to be considered; therefore, a method of bias elimination is described in Section 4.4.

383   4.4 R_W estimation for the whole UK

384   The R_W at Chilbolton station showed obvious systematic deviations compared with the
385   disdrometer-derived results (see Section 4.2 and 4.3). Simple bias correction was therefore
386   applied to adjust the individual storm KE estimations of R_W. The biases from dividing average
387     $R_{W-Morrison}$, R_{W-WDM6}, and R_{W-TAA} by average R_D during 2014-2017 were 0.55, 0.20, and 0.36,
388   respectively.

389   The rainfall erosivity distribution for the whole UK was then obtained. Figure 9 shows
390   the distribution of R_W at the annual scale covering the period 2013–2017. The pattern of the
391   rainfall erosivity maps showed a general regional-dominant characteristic. For example, it
392   always decreased from west to east, predominantly shaped by orography. Affected by the
393   prevailing westerly winds, there was abundant rainfall in the western and northern mountains, as
394   indicated by high rainfall KE values in these regions. In addition, among the study years, 2014
395   and 2015 showed higher national rainfall erosivity, with a large range in the west coast area.

396   Figure 10 shows the average R distribution for 2013–2017 estimated by rain gauges and
397   WRF MPs. WRF grids could cover all regions in the UK evenly, offering more detailed erosivity
398   results, especially in the mountainous northwestern region. Here, values of average R map
399   calculated by rain gauges were much higher than three types of R_W, although they all have R
400   decreased from west to east. Noted that $ke–I$ empirical equation at Chilbolton station used in the
401   whole UK, will not always be accurate in regions with different rainfall characteristics. In terms
402   of R_W results, the three MPs obtained the same spatial pattern in rainfall erosivity, where R_{W-WDM6}
403   yielded the greatest geographical difference. It is clear that the proposed WRF-based estimated
404   method can capture more details of the spatial change of rainfall erosivity compared with the
405   traditional disdrometer-based method.

406   The highest rainfall erosivity regions in the UK are concentrated in the mountainous
407   areas along the western coast, related to their rainfall system. The moist air brought by the
408   prevailing westerly wind from the Atlantic Ocean moves from west to east across the UK and
409   rises when it encounters the mountains of western England. Therefore, the mountainous regions
410   along the UK western coast have the highest rainfall amount and rainfall erosivity in the UK. In
411   addition, western Scotland is under the subpolar oceanic climate, which enhances its humidity.

412 On the contrary, eastern Scotland and northeastern England are more likely to expose continental

413 polar air mass, which brings dry and cold air and lower rainfall erosivity.

414   To evaluate the change in rainfall erosivity with time in the UK, the average value of all

415 the WRF grids covering the whole UK was calculated over 2013–2017 (Figure 11). The average

416 R_W trends of $R_{W\text{-}Morrison}$ and $R_{W\text{-}TAA}$ were similar, both increasing from a minimum in 2013 to a

417 maximum in 2014, and then gradually decreasing from 2014 to 2017. The red line in Figure 11

418 indicates a series of mean values of the three MPs results, which varied from 36,782 to 51,600

419 MJ mm ha^{-1} h^{-1} y^{-1} (mean: 43,216 MJ mm ha^{-1} h^{-1} y^{-1}).

420   The maximum values for $R_{W\text{-}Morrison}$ and $R_{W\text{-}TAA}$ occurred in 2014, whereas that of $R_{W\text{-}WDM6}$

421 occurred in 2015. A sequence of extreme weather events occurred in the UK in 2014, including

422 major winter storms in late January to mid-February, which caused widespread flooding and

423 other economic losses, and greatly increased rainfall erosivity that year. However, the gauge-

424 based interpolation map shows the average annual rainfall amount for the years 2013–2017 were

425 884.9, 1014.0, 1008.5, 894.9, and 937.3 mm, respectively. The large rainfall erosivity difference

426 between 2014 and 2015, and the two years with similar rainfall amount, indicates that much

427 rainfall erosion occurs during the rainfall events of high intensity instead of simply high rainfall

428 amount. A more notable variation pattern of rainfall erosivity may be found with longer

429 simulation. The strength of the proposed method lies on its ability to estimate large covering and

430 long-term rainfall erosivity.

431 **5 Discussion and conclusions**

432   This study presented a novel method for large-scale rainfall KE and erosivity estimation

433 based on high-resolution, WRF-derived DSDs. Three microphysical parameterizations schemes

434 (Morrison, WDM6, and Thompson aerosol-aware [TAA]) were designed to obtain raindrop size

435 distributions, rainfall KE and rainfall erosivity for the entire of the UK covering the period of

436 2013–2017. With validation from the long-term observations of a disdrometer, the WRF-based

437 rainfall erosivity exhibited an acceptable performance at Chilbolton station. Among the three

438 WRF schemes, TAA exhibited the most superior performance and was recommended for future

439 investigation. The results revealed that high rainfall erosivity occurred in the west coast area of

440 the UK. Compared with the traditional empirical method, the proposed method can explain

441 rainfall erosivity from a microphysical perspective and reflect more spatial variation because of

442 changes in rainfall KE at the whole-country scale. Therefore, the development of a numerical
443 weather prediction model offers an opportunity to better understand rainfall erosivity directly
444 from its true definition. More importantly, because the WRF model is able to be driven by the
445 global reanalysis data to obtain large-scale rainfall kinetic information, the proposed scheme can
446 be easily applied to other regions, especially in ungauged areas.

447 Although an acceptable rainfall erosivity estimation is obtained using the WRF model,
448 some uncertainties associated with it cannot be ignored. For example, as the MPs of WRF were
449 closely related to DSD, improper determination of MPs will introduce additional uncertainty.
450 The marked discrepancy among the three schemes (especially between Morrison and the others)
451 in this study underscored the possible uncertainty associated with R_W. The reliability of the WRF
452 model is heavily dependent on the model-driving initial data provided by mesoscale or global
453 models and complicated scheme setting and parameter adjustment (Liu et al., 2013; Thompson
454 and Eidhammer, 2014; Kumar et al., 2017). However, numerous uncertainties are observed in the
455 parameterization of the WRF simulation, and the choice of microphysical schemes has a
456 significant influence on the inverted DSD (Ćurić et al., 2009; Yang et al., 2019). Therefore,
457 combining the DSDs obtained by an increasing number of disdrometers and the WRF model is
458 valuable. For example, the Disdrometer Verification Network (DiVeN) in the UK (Pickering et
459 al., 2019) started in Feb 2017 can be introduced to support and improve our estimation in future
460 studies. Moreover, the measurement error by disdrometer may also contaminate the evaluation
461 process. For example, when comparing the observed raindrop velocities based on the
462 disdrometer at Bristol station with their empirical values, we observed dispersion of raindrops,
463 with a number of drops showing significant deviations. This velocity distribution resulted in
464 uncertainty in *ke* estimation.

465 Soil erosion in the UK is dominated by water erosion (10–30 t km^{-2} yr^{-1}), especially in
466 areas with abundant rainfall in Scotland, where the soil loss rate is approximately 5–10 times that
467 of dry areas (Duck, 1996). Thus, it is significant to estimate rainfall erosivity to elucidate the
468 microphysical characteristics of rainfall and rainfall–soil interactions. Benaud et al. (2020)
469 collated empirical soil erosion observations from UK-based studies into a geodatabase. However,
470 there is a limitation that this database does not cover the entirety of the UK, especially the
471 limited records in northern Scotland. In our future work, we propose to compare the soil loss
472 database with our estimated soil loss using WRF DSD based rainfall erosivity and a soil erosion

473   model (such as RUSLE). We believe that not only can we better analyze the impact of rainfall
474   and rainfall erosivity on the UK soil loss, but also help to better understand microphysical
475   rainfall–soil interactions to support the rational formulation of soil and water conservation
476   planning.

477   In addition, other sources of uncertainty, such as temporal downscaling of rainfall and
478   point-to-area representative error by WRF, may introduce further uncertainty. This should be put
479   in perspective of future work. It is expected that further exploration of research areas with
480   different climatic and geographical characteristics would help us to establish a greater degree of
481   accuracy on this matter.

482   **Author contributions**

483   QD and JZ carried out the experiments, analyzed the data, and prepared the manuscript
484   with contributions from all the co-authors. SLZ modified the text and provided financial support.
485   SNZ carried out quality checks of WRF. GL and DH principally conceived the idea and design
486   of the study.

487   **Competing interests**

488   The authors declare that they have no conflict of interest.

489   **Acknowledgments**

References

Alewell, C., Egli, M. and Meusburger, K. (2015). An attempt to estimate tolerable soil erosion rates by matching soil formation with denudation in Alpine grasslands. Journal of Soils and Sediments 15(6): 1383-1399.

Angulo-Mart ńez, M. and Barros, A. (2015). Measurement uncertainty in rainfall kinetic energy and intensity relationships for soil erosion studies: An evaluation using PARSIVEL disdrometers in the Southern Appalachian Mountains. Geomorphology 228: 28-40.

Angulo-Mart ńez, M., Beguer á, S. and Kysel ý, J. (2016). Use of disdrometer data to evaluate the relationship of rainfall kinetic energy and intensity (KE-I). Science of the Total Environment 568: 83-94.

Angulo-Martinez, M., Beguer á, S., Navas, A. and Machin, J. (2012). Splash erosion under natural rainfall on three soil types in NE Spain. Geomorphology 175: 38-44.

Atlas, D., Srivastava, R. and Sekhon, R. S. (1973). Doppler radar characteristics of precipitation at vertical incidence. Reviews of Geophysics 11(1): 1-35.

Atlas, D. and Ulbrich, C. W. (1977). Path-and area-integrated rainfall measurement by microwave attenuation in the 1–3 cm band. Journal of Applied Meteorology 16(12): 1322-1331.

Beard, K. V. (1976). Terminal velocity and shape of cloud and precipitation drops aloft. Journal of the Atmospheric Sciences 33(5): 851-864.

Benaud, P., Anderson, K., Evans, M., Farrow, L., Glendell, M., James, M. R., ... & Brazier, R. E. (2020). National-scale geodata describe widespread accelerated soil erosion. Geoderma, 371: 114378.

Bilotta, G., Grove, M. and Mudd, S. (2012). Assessing the significance of soil erosion. Transactions of the Institute of British Geographers 37(3): 342-345.

Bonta, J. (2004). Development and utility of Huff curves for disaggregating precipitation amounts. Applied Engineering in Agriculture 20(5): 641.

Borrelli, P., Robinson, D. A., Fleischer, L. R., Lugato, E., Ballabio, C., Alewell, C., Meusburger, K., Modugno, S., Sch ütt, B. and Ferro, V. (2017). An assessment of the global impact of 21st century land use change on soil erosion. Nature Communications 8(1): 1-13.

528 Brown, B. R., Bell, M. M. and Frambach, A. J. (2016). Validation of simulated hurricane drop
529 size distributions using polarimetric radar. Geophysical Research Letters 43(2): 910-917.

530 Brown, L. and Foster, G. (1987). Storm erosivity using idealized intensity distributions.
531 Transactions of the ASAE 30(2): 379-386.

532 Carter, C. E., Greer, J., Braud, H. and Floyd, J. (1974). Raindrop characteristics in south central
533 United States. Transactions of the ASAE 17(6): 1033-1037.

534 Cintineo, R., Otkin, J. A., Xue, M. and Kong, F. (2014). Evaluating the performance of planetary
535 boundary layer and cloud microphysical parameterization schemes in convection-permitting
536 ensemble forecasts using synthetic GOES-13 satellite observations. Monthly Weather Review
537 142(1): 163-182.

538 Ćurić, M., Janc, D., Vučković, V. and Kovačević, N. (2009). The impact of the choice of the
539 entire drop size distribution function on Cumulonimbus characteristics. Meteorologische
540 Zeitschrift 18(2): 207-222.

541 Dai, Q. and Han, D. (2014). Exploration of discrepancy between radar and gauge rainfall
542 estimates driven by wind fields. Water Resources Research 50(11): 8571-8588.

543 Dai, Q., Bray, M., Zhuo, L., Islam, T., and Han, D. (2017). A scheme for raingauge network
544 design based on remotely-sensed rainfall measurements. Journal of Hydrometeorology 18: 363-
545 379.

546 Dai, Q., Yang, Q., Han, D., Rico‐Ramirez, M. A., and Zhang, S. (2019). Adjustment of radar‐
547 gauge rainfall discrepancy due to raindrop drift and evaporation using the Weather Research and
548 Forecasting model and dual-polarization radar. Water Resources Research 55: 9211–9233.

549 Davison, P., Hutchins, M., Anthony, S., Betson, M., Johnson, C. and Lord, E. (2005). The
550 relationship between potentially erosive storm energy and daily rainfall quantity in England and
551 Wales. Science of the Total Environment 344(1-3): 15-25.

552 De Roo, A., Wesseling, C. and Ritsema, C. (1996). LISEM: a single‐event physically based
553 hydrological and soil erosion model for drainage basins. I: theory, input and output. Hydrological
554 Processes 10(8): 1107-1117.

555 Dee, D. P., Uppala, S., Simmons, A., Berrisford, P., Poli, P., Kobayashi, S., Andrae, U.,

556 Balmaseda, M., Balsamo, G. and Bauer, d. P. (2011). The ERA‐Interim reanalysis:

557 Configuration and performance of the data assimilation system. Quarterly Journal of the Royal

558 Meteorological Society 137(656): 553-597.

559 Defra (2009). Safeguarding our soils–A strategy for England. Defra, UK.

560 Doelling, I. G., Joss, J. and Riedl, J. (1998). Systematic variations of Z–R-relationships from

561 drop size distributions measured in northern Germany during seven years. Atmospheric Research

562 47: 635-649.

563 Duck, R. W. (1996). Regional variations of fluvial sediment yield in eastern Scotland. Erosion

564 and Sediment Yield: Global and Regional Perspectives 236:157-161.

565 Dudhia, J. (1989). Numerical study of convection observed during the winter monsoon

566 experiment using a mesoscale two-dimensional model. Journal of the Atmospheric Sciences

567 46(20): 3077-3107.

568 EA (2004). The state of soils in England and Wales. Environment Agency, UK.

569 Ek, M., Mitchell, K., Lin, Y., Rogers, E., Grunmann, P., Koren, V., Gayno, G. and Tarpley, J.

570 (2003). Implementation of Noah land surface model advances in the National Centers for

571 Environmental Prediction operational mesoscale Eta model. Journal of Geophysical Research:

572 Atmospheres 108(22):8851.

573 Evans, R. (1990). Soils at risk of accelerated erosion in England and Wales. Soil use and

574 Management 6(3): 125-131.

575 Fornis, R. L., Vermeulen, H. R. and Nieuwenhuis, J. D. (2005). Kinetic energy–rainfall intensity

576 relationship for Central Cebu, Philippines for soil erosion studies. Journal of Hydrology 300(1-4):

577 20-32.

578 Gilmore, M. S., Straka, J. M. and Rasmussen, E. N. (2004). Precipitation uncertainty due to

579 variations in precipitation particle parameters within a simple microphysics scheme. Monthly

580 Weather Review 132(11): 2610-2627.

581 Hanel, M., Máca, P., Bašta, P., Vlnas, R. and Pech, P. (2016). The rainfall erosivity factor in the

582 Czech Republic and its uncertainty. Hydrology and Earth System Sciences 20(10): 4307-4322.

583 Hong, S.-Y., Lim, K.-S. S., Lee, Y.-H., Ha, J.-C., Kim, H.-W., Ham, S.-J. and Dudhia, J. (2010).
584 Evaluation of the WRF double-moment 6-class microphysics scheme for precipitating
585 convection. Advances in Meteorology 2010.

586 Hudson, N. (1963). Raindrop size distribution in high intensity storms. Rhodesian Journal of
587 Agricultural Research 1(1): 6-11.

588 Islam, T., Rico-Ramirez, M. A., Thurai, M. and Han, D. (2012). Characteristics of raindrop
589 spectra as normalized gamma distribution from a Joss–Waldvogel disdrometer. Atmospheric
590 Research 108: 57-73.

591 Janjić, Z. I. (1994). The step-mountain eta coordinate model: Further developments of the
592 convection, viscous sublayer, and turbulence closure schemes. Monthly Weather Review 122(5):
593 927-945.

594 Johnson, M., Jung, Y., Dawson, D. T. and Xue, M. (2016). Comparison of simulated
595 polarimetric signatures in idealized supercell storms using two-moment bulk microphysics
596 schemes in WRF. Monthly Weather Review 144(3): 971-996.

597 Jones, D. M. A. (1959). The shape of raindrops. Journal of the Atmospheric Sciences 16(1): 511-
598 515.

599 Jung, Y., Xue, M. and Zhang, G. (2010). Simulations of polarimetric radar signatures of a
600 supercell storm using a two-moment bulk microphysics scheme. Journal of Applied Meteorology
601 and Climatology 49(1): 146-163.

602 Kain, J. S. (2004). The Kain–Fritsch convective parameterization: an update. Journal of Applied
603 Meteorology 43(1): 170-181.

604 Kinnell, P. (1981). Rainfall intensity-kinetic energy relationships for soil loss prediction. Soil
605 Science Society of America Journal 45(1): 153-155.

606 Kinnell, P. and Risse, L. (1998). USLE-M: empirical modeling rainfall erosion through runoff
607 and sediment concentration. Soil Science Society of America Journal 62(6): 1667-1672.

608 Lim, K.-S. S. and Hong, S.-Y. (2010). Development of an effective double-moment cloud
609 microphysics scheme with prognostic cloud condensation nuclei (CCN) for weather and climate
610 models. Monthly Weather Review 138(5): 1587-1612.

611 Lim, Y. S., Kim, J. K., Kim, J. W., Park, B. I. and Kim, M. S. (2015). Analysis of the
612 relationship between the kinetic energy and intensity of rainfall in Daejeon, Korea. Quaternary
613 International 384: 107-117.

614 Marshall, J. S. and Palmer, W. M. K. (1948). The distribution of raindrops with size. Journal of
615 Meteorology 5(4): 165-166.

616 McIsaac, G. (1990). Apparent geographic and atmospheric influences on raindrop sizes and
617 rainfall kinetic energy. Journal of Soil and Water Conservation 45(6): 663-666.

618 Meshesha, D. T., Tsunekawa, A. and Haregeweyn, N. (2019). Influence of raindrop size on
619 rainfall intensity, kinetic energy, and erosivity in a sub-humid tropical area: a case study in the
620 northern highlands of Ethiopia. Theoretical and Applied Climatology 136(3-4): 1221-1231.

621 Meshesha, D. T., Tsunekawa, A., Tsubo, M., Haregeweyn, N. and Adgo, E. (2014). Drop size
622 distribution and kinetic energy load of rainfall events in the highlands of the Central Rift Valley,
623 Ethiopia. Hydrological Sciences Journal 59(12): 2203-2215.

624 Meshesha, D. T., Tsunekawa, A., Tsubo, M., Haregeweyn, N. and Tegegne, F. (2016).
625 Evaluation of kinetic energy and erosivity potential of simulated rainfall using Laser
626 Precipitation Monitor. Catena 137: 237-243.

627 Mikoš, M., Jošt, D. and Petkovšek, G. (2006). Rainfall and runoff erosivity in the alpine climate
628 of north Slovenia: a comparison of different estimation methods. Hydrological sciences journal
629 51(1): 115-126.

630 Mlawer, E. J., Taubman, S. J., Brown, P. D., Iacono, M. J. and Clough, S. A. (1997). Radiative
631 transfer for inhomogeneous atmospheres: RRTM, a validated correlated‐k model for the
632 longwave. Journal of Geophysical Research: Atmospheres 102(14): 16663-16682.

633 MO (2012). Met Office Integrated Data Archive System (MIDAS) land and marine surface
634 stations data (1853‐current).

635 Montopoli, M., Marzano, F. S. and Vulpiani, G. (2008). Analysis and synthesis of raindrop size
636 distribution time series from disdrometer data. IEEE Transactions on Geoscience and Remote
637 Sensing 46(2): 466-478.

638 Morgan, R. (1985). Assessment of soil erosion risk in England and Wales. Soil use and
639 Management 1(4): 127-131.

640 Morrison, H., Milbrandt, J. A., Bryan, G. H., Ikeda, K., Tessendorf, S. A. and Thompson, G.
641 (2015). Parameterization of cloud microphysics based on the prediction of bulk ice particle
642 properties. Part II: Case study comparisons with observations and other schemes. Journal of the
643 Atmospheric Sciences 72(1): 312-339.

644 Morrison, H., Thompson, G. and Tatarskii, V. (2009). Impact of cloud microphysics on the
645 development of trailing stratiform precipitation in a simulated squall line: Comparison of one-
646 and two-moment schemes. Monthly weather review 137(3): 991-1007.

647 Nyssen, J., Vandenreyken, H., Poesen, J., Moeyersons, J., Deckers, J., Haile, M., Salles, C. and
648 Govers, G. (2005). Rainfall erosivity and variability in the Northern Ethiopian Highlands.
649 Journal of Hydrology 311(1-4): 172-187.

650 O'Neill, D. (2007). The total external environmental costs and benefits of agriculture in the UK.
651 Environment Agency, UK.

652 Panagos, P., Ballabio, C., Borrelli, P., Meusburger, K., Klik, A., Rousseva, S., Tadić, M. P.,
653 Michaelides, S., Hrabalќová, M. and Olsen, P. (2015a). Rainfall erosivity in Europe. Science of
654 the Total Environment 511: 801-814.

655 Panagos, P., Borrelli, P., Poesen, J., Ballabio, C., Lugato, E., Meusburger, K., Montanarella, L.
656 and Alewell, C. (2015b). The new assessment of soil loss by water erosion in Europe.
657 Environmental Science & Policy 54: 438-447.

658 Park, S., Mitchell, J. and Bubenzer, G. (1982). Splash erosion modeling: physical analysis.
659 Transactions of the ASAE 25:357-361.

660 Petan, S., Rusjan, S., Vidmar, A. and Mikoš, M. (2010). The rainfall kinetic energy–intensity
661 relationship for rainfall erosivity estimation in the mediterranean part of Slovenia. Journal of
662 Hydrology 391(3-4): 314-321.

663 Pickering, B. S., Neely III, R. R., & Harrison, D. (2019). The Disdrometer Verification Network
664 (DiVeN): a UK network of laser precipitation instruments. Atmospheric Measurement
665 Techniques 12: 5845-5861.

666 Prigent, C. (2010). Precipitation retrieval from space: An overview. Comptes Rendus Geoscience
667 342(4-5): 380-389.

668 Renard, K. G., Foster, G. R., Weesies, G., McCool, D. and Yoder, D. (1997). Predicting soil
669 erosion by water: a guide to conservation planning with the Revised Universal Soil Loss
670 Equation (RUSLE), United States Department of Agriculture Washington, DC.

671 Rosewell, C. J. (1986). Rainfall kinetic energy in eastern Australia. Journal of Climate and
672 Applied Meteorology 25(11): 1695-1701.

673 Sanchez-Moreno, J. F., Mannaerts, C. M., Jetten, V. and Löffler-Mang, M. (2012). Rainfall
674 kinetic energy–intensity and rainfall momentum–intensity relationships for Cape Verde. Journal
675 of Hydrology 454: 131-140.

676 Sempere‐Torres, D., Porrà, J. M. and Creutin, J. D. (1998). Experimental evidence of a general
677 description for raindrop size distribution properties. Journal of Geophysical Research:
678 Atmospheres 103(2): 1785-1797.

679 Song, Y., Han, D. and Rico-Ramirez, M. A. (2017). High temporal resolution rainfall rate
680 estimation from rain gauge measurements. Journal of Hydroinformatics 19(6): 930-941.

681 Thompson, G. and Eidhammer, T. (2014). A study of aerosol impacts on clouds and precipitation
682 development in a large winter cyclone. Journal of the Atmospheric Sciences 71(10): 3636-3658.

683 Uplinger, W. (1981). A new formula for raindrop terminal velocity. Conference on Radar
684 Meteorology, 20 th, Boston, MA.

685 Van Dijk, A., Bruijnzeel, L. and Rosewell, C. (2002). Rainfall intensity–kinetic energy
686 relationships: a critical literature appraisal. Journal of Hydrology 261(1-4): 1-23.

687 Wang, L., Shi, Z., Wang, J., Fang, N., Wu, G. and Zhang, H. (2014). Rainfall kinetic energy
688 controlling erosion processes and sediment sorting on steep hillslopes: a case study of clay loam
689 soil from the Loess Plateau, China. Journal of Hydrology 512: 168-176.

690 Weiss, L. L. (1964). Ratio of true to fixed-interval maximum rainfall. Journal of the Hydraulics
691 Division 90(1): 77-82.

692 Williams, R. and Sheridan, J. (1991). Effect of rainfall measurement time and depth resolution
693 on EI calculation. Transactions of the ASAE 34(2): 402-0406.

694 Wischmeier, W. H. and Smith, D. D. (1958). Rainfall energy and its relationship to soil loss. Eos,
695 Transactions American Geophysical Union 39(2): 285-291.

696 Wischmeier, W. H. and Smith, D. D. (1978). Predicting rainfall erosion losses-a guide to
697 conservation planning. Department of Agriculture, Science and Education Administration, US.

698 Xie, Y., Yin, S., Liu, B., Nearing, M. A. and Zhao, Y. (2016). Models for estimating daily
699 rainfall erosivity in China. Journal of Hydrology 535: 547-558.

700 Yang, Q., Dai, Q., Han, D., Chen, Y., and Zhang, S. (2019). Sensitivity analysis of raindrop size
701 distribution parameterizations in weather research and forecasting rainfall simulation.
702 Atmospheric Research 228:1-13.

703
704

705
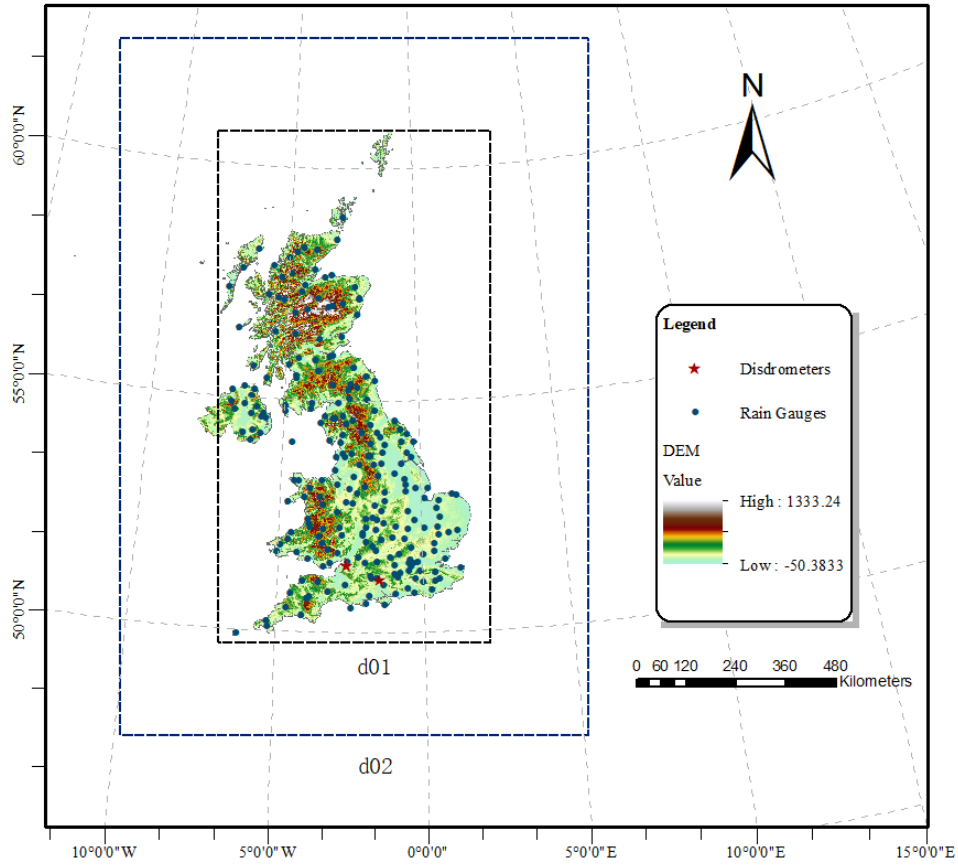
Figure 1. Location of rain gauges, Joss–Waldvogel disdrometer (JWD) at Chilbolton Observatory, OTT Parsivel[2] disdrometer (OPD) at Bristol Observatory and configurations of domain setups in the WRF model.
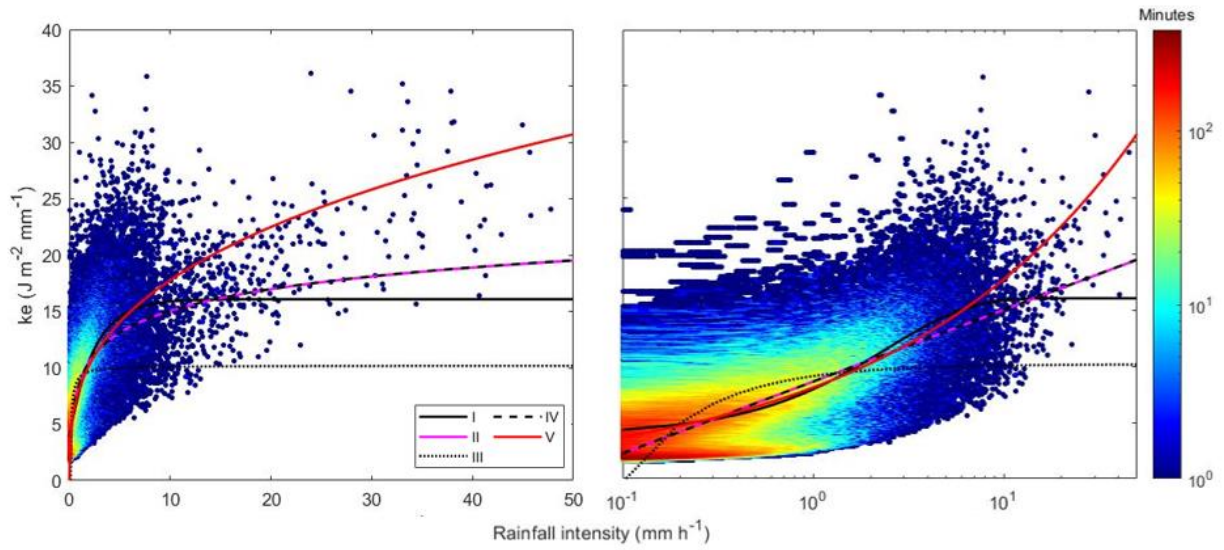
Figure 2. Minutes number per intensity class (x-axis) and *ke* class (y-axis) with five fitted *ke–I* curves at Chilbolton station (2004–2013), plotted on linear (left) and logarithmic (right) intensity scales.
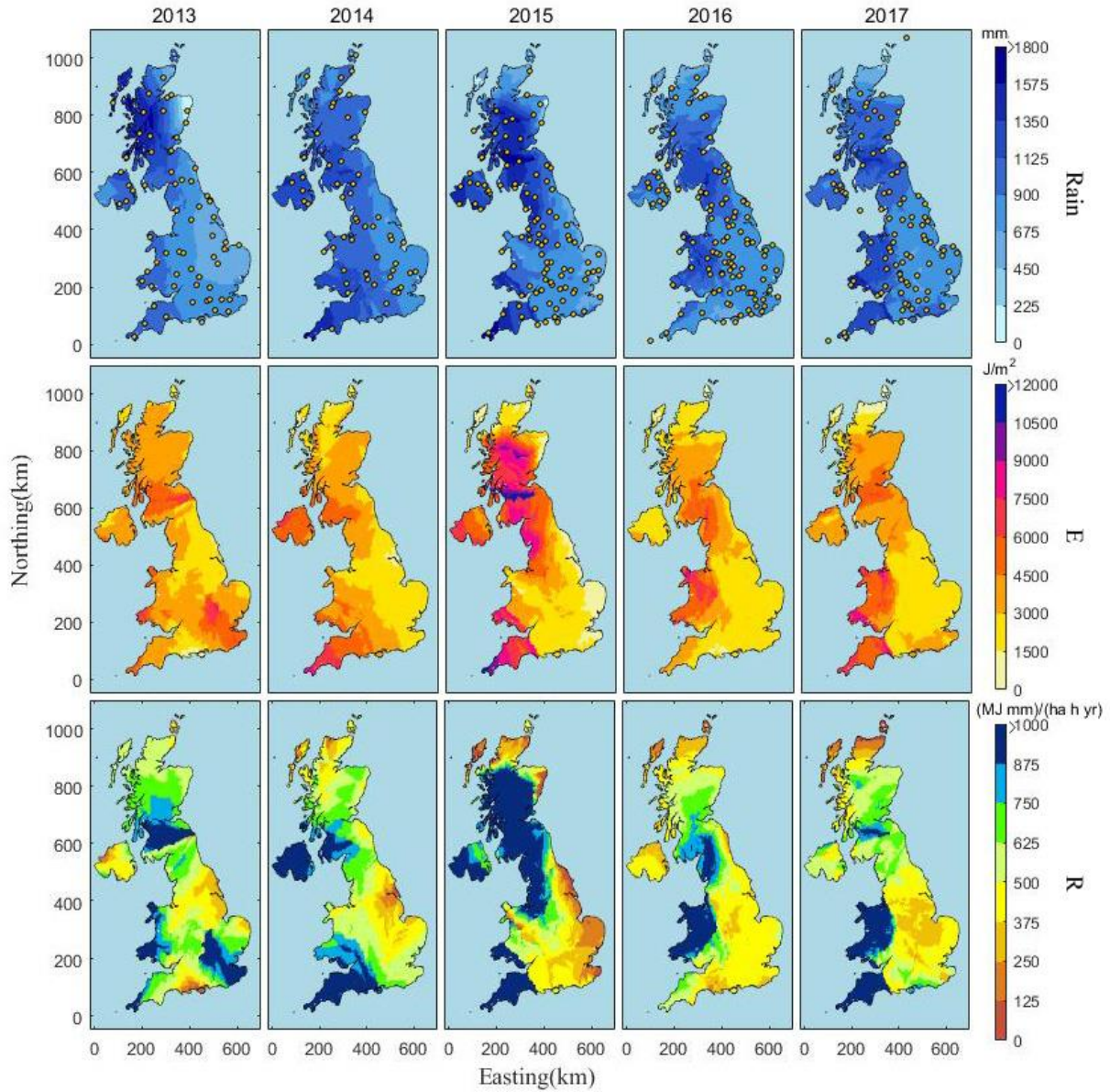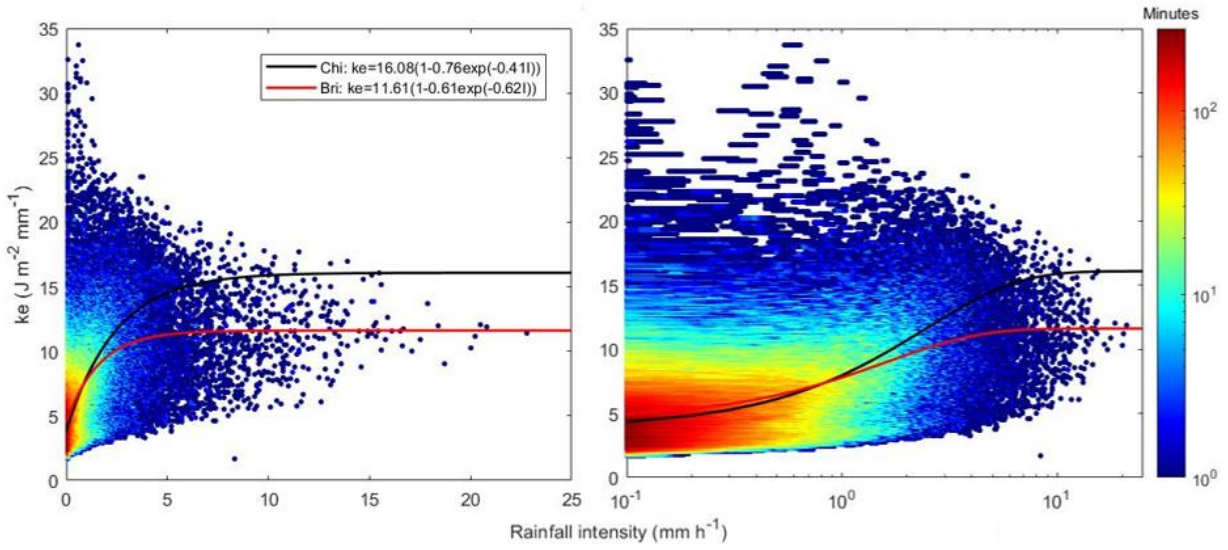
Figure 3. Gauge-based interpolation maps of annual rainfall amount (*Rain*), rainfall kinetic energy (*E*) and rainfall erosivity (*R*) in 2013–2017.

719

Figure 4. Minutes number per intensity class (x-axis) and ke class (y-axis) with fitted *ke–I* curves at Bristol station (2015–2018), plotted on linear (left) and logarithmic (right) intensity scales.

724
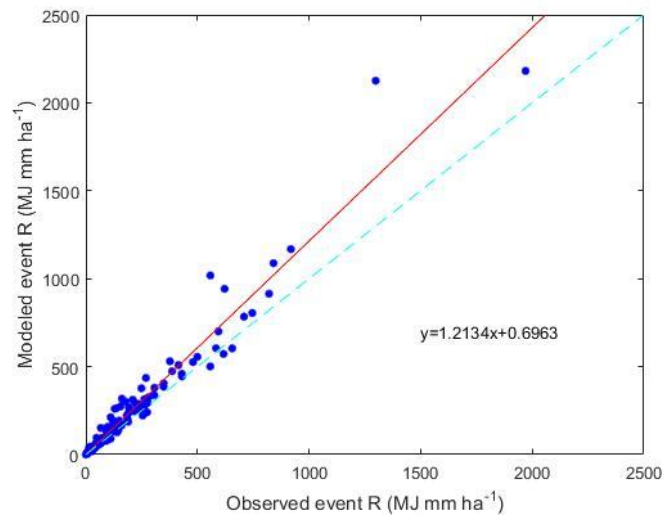
Figure 5. Comparison of observed and modeled event rainfall erosivity at Bristol Station, covering the period of 2016–2019.

725

726

727

728
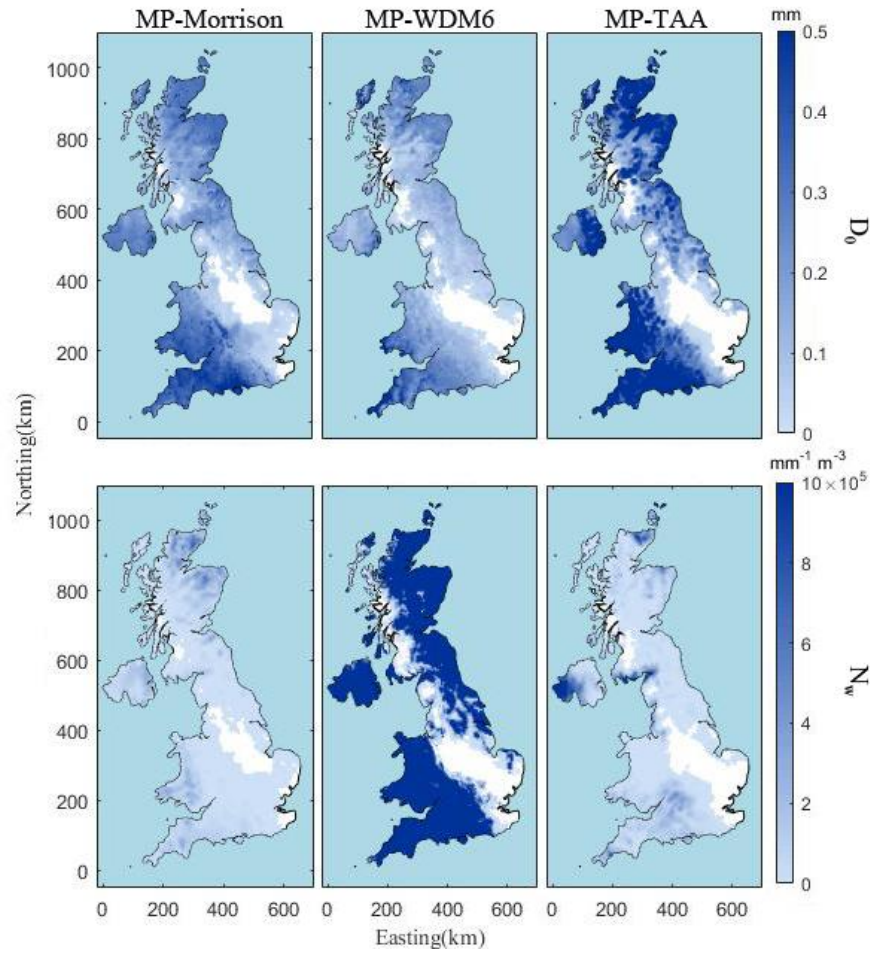
Figure 6. Map of average WRF DSD D_0 and N_w (January 10, 2013).
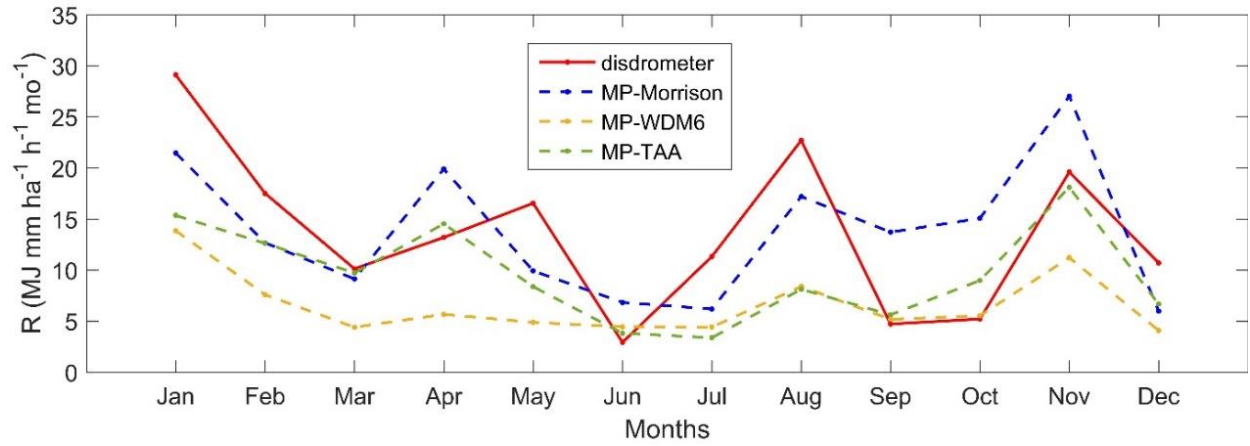
730

731
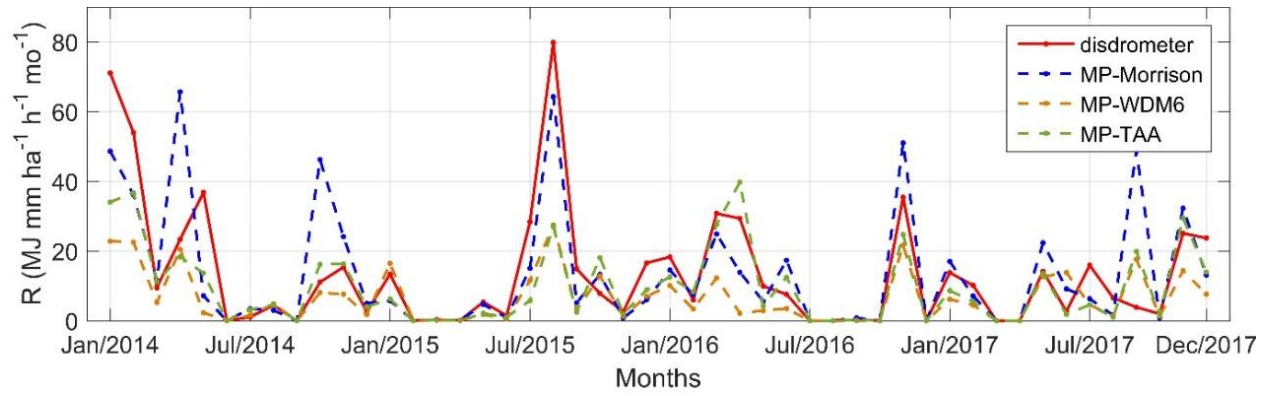
Figure 7. Comparison of disdrometer- and WRF-derived monthly rainfall erosivity estimations at Chilbolton station (2014–2017).
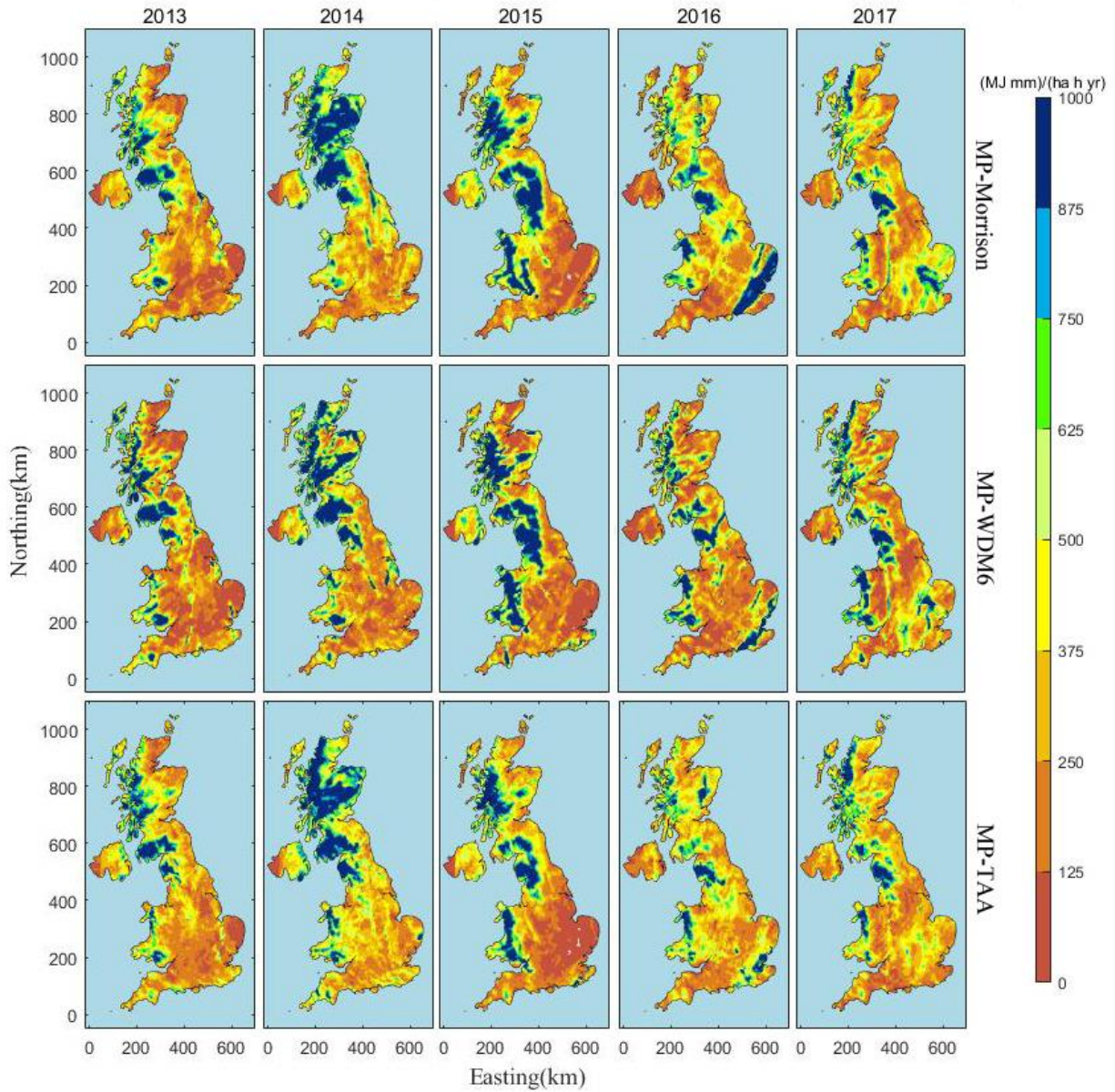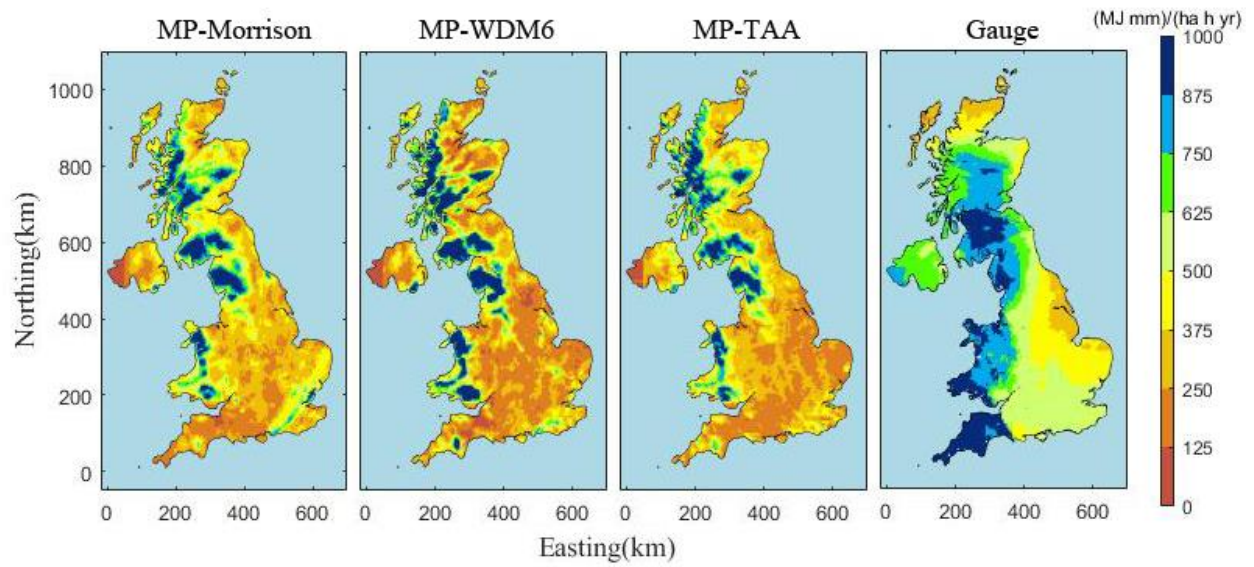
734

735

Figure 8. Comparison of disdrometer- and WRF-derived average monthly rainfall erosivity estimations at Chilbolton station (2014–2017).

738

739
740 **Figure 9**. WRF-derived annual rainfall erosivity maps of the whole UK for different years.
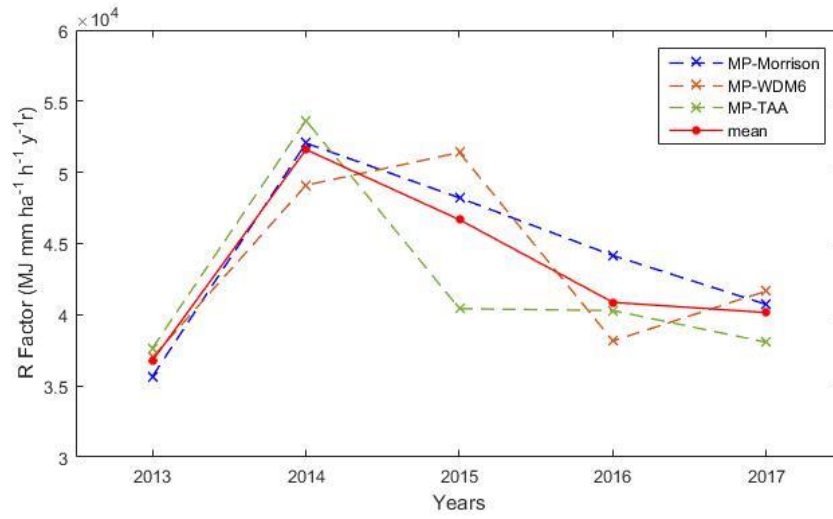
741

Figure 10. The 5-year (2013–2017) average annual rainfall erosivity maps based on WRF grids and rain gauge interpolation.

746

Figure 11. WRF-derived average annual rainfall erosivity of all the WRF grids covering the whole UK (2013–2017).

747

748

749

750   **Table 1.** Relationship of ke–I at Chilbolton Station (2004–2013).

ID	Equation	Calibration R^2	Validation R^2
I	$ke = 16.08(1 - 0.76e^{-0.41I})$	0.50	0.45
II	$ke = 8.65 + 6.39\lg(I)$	0.48	0.43
III	$ke = 10.19 - 1.05/I$	0.29	0.25
IV	$ke = 8.65 + 2.78\ln(I)$	0.48	0.43
V	$ke = 8.12I^{0.34}$	0.50	0.45

751

752

753 **Table 2.** The configurations of WRF model for two nested domains.

Domain	Domain size (km)	Grid Spacing (km)	Grid size	Downscaling ratio
d01	$1,125 \times 1,675$	25	45×67	-
d02	$655 \times 1,230$	5	131×246	1:5

754

755

756 **Table 3**. Indicators comparison between disdrometer-derived rainfall erosivity R_D and three

757 types of WRF-derived rainfall erosivity at Chilbolton station on monthly scale (2014-2017).

Indicators	MP-Morrison	MP-WDM6	MP-TAA
Pearson	0.71	0.77	0.79
MAE	8.05	8.42	6.51
R^2	0.42	0.31	0.54

758